AIP Advances

RESEARCH ARTICLE | OCTOBER 22 2026

# Energy levels analysis of magnetron sputtered $MoO_x$ thin films

Nico Ruskaup ; Konstantin Rücker ; Kai Gehrke ; Stephan Heise ; Martin Vehse

Check for updates

*AIP Advances* 16, 105305 (2026)
https://doi.org/10.1063/6.0005792

View Online
Export Citation

## Articles You May Be Interested In

Interfacial electronic structure at the $CH_3NH_3PbI_3/MoO_x$ interface

*Appl. Phys. Lett.* (May 2015)

Molybdenum oxide $MoO_x$: A versatile hole contact for silicon solar cells

*Appl. Phys. Lett.* (December 2014)

Towards industrial deposition of metal oxides for passivating and carrier selective contacts: $MoO_x$ deposited by industrial size reactive DC magnetron sputtering and industrial size linear evaporation source

*AIP Conf. Proc.* (August 2018)

04 November 2026 11:40:56

AIP Publishing
Special Topics Open for Submissions
Learn More

AIP Publishing

# Energy levels analysis of magnetron sputtered $MoO_x$ thin films

Cite as: AIP Advances 16, 105305 (2026); doi: 10.1063/6.0005792
Submitted: 28 August 2026 • Accepted: 9 October 2026 •
Published Online: 22 October 2026

View Online Export Citation CrossMark

Nico Ruskaup,[1,a)] Konstantin Rücker,[2] Kai Gehrke,[1] Stephan Heise,[3] and Martin Vehse[1]

## AFFILIATIONS

[1] Deutsches Zentrum für Luft- und Raumfahrt (DLR), Institut für Vernetzte Energiesysteme, Carl-von-Ossietzky-Straße 15, Oldenburg 26129, Germany
[2] Deutsches Zentrum für Luft- und Raumfahrt (DLR), Institut für Technische Thermodynamik, Carl-von-Ossietzky-Straße 15, Oldenburg 26129, Germany
[3] Deutsches Zentrum für Luft- und Raumfahrt (DLR), Institut für Solarforschung, Carl-von-Ossietzky-Straße 15, Oldenburg 26129, Germany

[a)] **Author to whom correspondence should be addressed:** nico.ruskaup@dlr.de

## ABSTRACT

Ultrathin molybdenum oxide films are promising as transparent carrier-selective layers in photovoltaic cells, yet the electronic structure of sputtered molybdenum oxide ($MoO_x$) and, therefore, the nature of electronic transport remains insufficiently understood. In this study, we show that magnetron-sputtered $MoO_x$ thin films exhibit a largely invariant energy-level structure across variations in thickness, target material, and underlying layer, while remaining electrically nonmetallic. Films with thicknesses of ≈5 nm and ≈20 nm were prepared from either a metallic molybdenum target in a reactive process or a ceramic $MoO_x$ target on glass and, for some samples, on germanium or aluminum doped zinc oxide coated glass. The results from Kelvin probe force microscopy, ultraviolet photoelectron spectroscopy, UV–Vis–NIR spectroscopy, optical modeling, and four-point probe measurements were combined to determine the work function, valence-band edge energy, optical bandgap, and derived conduction-band edge energy. Neither film thickness, target type, nor underlying layer seems to create a clear systematic shift of the energy levels. Additional occupied states were observed at binding energies of about 1.0–1.6 eV and are consistent with defect-related intra-gap states. The Fermi level is found to be ~0.1–0.5 eV above the conduction-band edge derived from the optical bandgap. The results are discussed with respect to the mechanisms underlying the carrier-selective transport in functional $MoO_x$ thin films.

*© 2026 Author(s). All article content, except where otherwise noted, is licensed under a Creative Commons Attribution (CC BY) license (https://creativecommons.org/licenses/by/4.0/).* https://doi.org/10.1063/6.0005792

04 November 2026 11:40:56

## I. INTRODUCTION

Semitransparent photovoltaics can be used in large glass areas in building facades not only for daylight and solar heat gain control but also for electricity generation.[1] Conventional solar-control glazing typically reduces solar heat gain in buildings through thin, optically functional coatings that reflect or absorb part of the incident radiation.[2] These coatings are manufactured industrially using large-area inline sputtering systems. This creates the possibility of using existing production infrastructure to manufacture semitransparent photovoltaic layer stacks, provided that all functional layers can be deposited using compatible sputtering processes.[3] Previous work has already shown that ultrathin sputtered germanium films can be used as absorbers in thin-film solar cells and that a sputtered absorber represents an important step toward fully sputtered semitransparent solar cells.[1] Furthermore, a fully sputtered layer stack with a thin germanium absorber was shown to provide nearly color-neutral transmission and suitable optical properties for facade applications.[4] In addition to the absorber and transparent conductive oxides, carrier-selective contacts are important for the operation of such a device.[5]

Some transition-metal oxides are particularly attractive for this purpose because they achieve wide bandgaps, low parasitic absorption in the visible spectral range, and suitable energy levels for selective carrier extraction.[6,7] Molybdenum oxide is frequently discussed as a hole-selective contact material.[8–10] Its electronic structure depends strongly on its composition. Stoichiometric $MoO_3$ is a wide-bandgap oxide with high transparency, a large work


© Author(s) 2026

function, and Mo centers with reduced oxidation states.[11] The resulting combination of high optical transparency and a defect-dependent electronic structure makes molybdenum oxide ($MoO_x$) an attractive material for transparent electronic contacts and functional layers.[12–14] An especially relevant technological context is the use of $MoO_x$ as a carrier-selective contact material in thin photovoltaic layer stacks without being dependent on doping.[15,16]

High work functions and a strong dependence of the electronic properties on oxygen stoichiometry, oxidation state, and defect structure have been reported for $MoO_x$.[17,18] Battaglia *et al.* demonstrated that ultrathin $MoO_x$ can be used as a transparent, dopant-free, hole-selective contact to n-type silicon and that it is characterized by a large work function and defect states within the bandgap.[10] The role of such defect states is particularly relevant for $MoO_x$ because oxygen vacancies and reduced Mo states can affect the work function, band alignment, and charge transport.[19,20] Further studies have shown that the defect distribution in $MoO_x$ depends on processing and post-treatment conditions and that both the work function and the defect density are key parameters governing the function of $MoO_x$ as a selective contact.[21]

Despite this prior work, the energy-level structure of sputtered $MoO_x$ thin films remains insufficiently understood, particularly in the context of fully sputtered solar cells. Many studies of $MoO_x$ as a selective contact are based on other deposition methods.[22,23] For a fully sputtered solar cell, however, sputter deposition of $MoO_x$ itself needs to be analyzed. The resulting film properties may differ from $MoO_x$ deposited by other techniques because the oxygen stoichiometry can be affected, thereby changing the electronic energy levels.[24] This can be attributed to the different energies of the incident ions, which are typically significantly higher in sputtering than in other deposition methods, such as evaporation. This is particularly relevant for films only a few nanometers thick, as used for contact layers in solar-cell stacks, where interface effects dominate the resulting electronic properties. In a previously modeled fully sputtered layer stack, $MoO_x$ and $TiO_x$ were already considered as selective contact materials with a $MoO_x$ thickness of ~5 nm.[4]

The research objective of this work is to gain a better understanding of the transport of charge-carrier-selective contact materials in the context of $MoO_x$ by investigating the energy levels. The $MoO_x$ films were deposited on glass and on underlying germanium or aluminum doped zinc oxide (AZO) relevant to a solar-cell stack in order to examine both intrinsic material properties and the influence of realistic layer configurations. These two underlying materials were chosen to simulate two different deposition methods for a potential future solar cell, in which either the hole-selective contact or the electron-selective contact is sputtered first. Depending on the order in which the layer stack is sputtered, either AZO or germanium serves as the underlying layer. In addition, two possible sputter processes were compared: reactive sputtering from a metallic Mo target and non-reactive sputtering from a ceramic $MoO_x$ target. This comparison is relevant because both approaches are technologically applicable but differ, especially in the need to introduce additional oxygen during sputtering when using the metallic target to achieve $MoO_x$. This could result in different oxygen stoichiometries and defect structures.[25,26]

The measurement results of Kelvin probe force microscopy (KPFM), ultraviolet photoelectron spectroscopy (UPS), and UV–Vis–NIR spectrophotometry were combined to determine the energy-level structure. KPFM was used to derive the relative work function or changes in the surface potential, whereas UPS provided the valence-band position and information on occupied states near the Fermi level. UV–Vis–NIR spectrophotometry was used to determine the optical bandgap. With this approach, a consistent energy-level diagram of the sputtered $MoO_x$ films was derived.

## II. EXPERIMENTAL DETAILS

### A. Sample preparation

Thin molybdenum oxide films were deposited on glass, glass/germanium, and glass/AZO substrates by magnetron sputtering. The sample preparation was designed to produce $MoO_x$ films with relevant thicknesses and sublayers, enabling the energetic positions of the work function, valence-band edge, optical bandgap, and conduction-band edge to be derived. A Vistaris 600 inline magnetron sputtering system from Singulus Technologies was used for the $MoO_x$ depositions. Two different processes and targets were used for the deposition of $MoO_x$: a metallic molybdenum target and a ceramic molybdenum oxide target. For deposition from the metallic molybdenum target, a planar Mo sputtering target with a purity of 99.95% from Avaluxe International was used. The films were deposited in a DC sputtering process at a sputtering power of 4 kW and a process pressure of ~$3.4 \times 10^{-3}$ mbar, using an oxygen plasma with an $O_2$ flow of 200 sccm.

For deposition from the ceramic molybdenum oxide target, a planar molybdenum oxide sputtering target with a purity of 99.9% from Avaluxe International was used. The target has a composition specified by the manufacturer of $MoO_x$, ranging from x = 2.7 to x = 2.8. The films were deposited in a DC sputtering process at a sputtering power of 1 kW and a process pressure of ~$4.5 \times 10^{-3}$ mbar, using a plasma generated from 300 sccm Ar and 20 sccm $O_2$.

For selected samples, an additional germanium or AZO interlayer was deposited between the glass and $MoO_x$. The sputtering parameters for the AZO and germanium layers are described elsewhere.[4]

The nominal $MoO_x$ film thicknesses were 5.4 and 21.6 nm. They were determined by measuring dedicated calibration samples with integer multiples of these thicknesses using a Bruker Dektak XT profilometer. The thinner film corresponds to the thickness range relevant for selective contacts in ultrathin photovoltaic layer stacks, whereas the thicker film enables a more robust determination of the optical and photoelectronic properties.

The resulting samples comprise different $MoO_x$ film thicknesses, substrates, and target types. This enables an assessment of whether observed changes or specific features are primarily caused by the film thickness, the substrates, or the sputtering route.

### B. KPFM measurements

Kelvin probe force microscopy measurements were performed to determine the local surface potential of the samples and to derive the effective work function of the $MoO_x$ surface. The measurements were performed using an NX10 system from Park Systems and an

04 November 2026 11:40:56


© Author(s) 2026

ElectriMulti75-G cantilever from BudgetSensors. Before measuring the $MoO_x$ samples, the measurement system was calibrated using a reference sample consisting of alternating aluminum and gold lines deposited on an oxide covered silicon substrate with a known work function. This allowed the measured contact potential difference between the probe tip and the sample to be converted into a relative or calibrated work function of the sample surface. As a surface probe, KPFM is a highly surface-sensitive measurement that is hardly affected by the thickness of the layers.

For each sample, a square area of 100 $\mu m^2$ was measured with 256 data points per scan line and a scan rate of 0.7 Hz. The median and other statistical measures of the surface potential were determined from the measured surface-potential maps. In addition, the KPFM measurement also records the z-height, which allows us to characterize the morphology.

### C. UPS measurements

The electronic structure of the $MoO_x$ films was analyzed by ultraviolet photoelectron spectroscopy (UPS). A helium lamp and the helium I line were used as the excitation source. The spectra were recorded at a pass energy of 1 eV, and 10 scans were accumulated for each measurement. The step size was 0.02 eV.

To determine the energetic position of the valence-band edge, the rising region of the valence band was fitted linearly. The intersection of the fitted line with the intensity baseline was taken as the valence-band maximum relative to the Fermi level.[27,28] All binding energies were referenced to the Fermi level. In addition, the near-Fermi-level region of the UPS spectra was analyzed to identify possible occupied states within the bandgap.

The KPFM measurements were performed under ambient conditions, whereas the UPS spectra were acquired under ultrahigh-vacuum conditions. Consequently, the two techniques may probe surfaces with different adsorbate coverages. These can modify the surface and, thus, the work function measured by KPFM, whereas desorption and surface equilibration under ultrahigh vacuum may result in a different surface potential during UPS analysis. The absolute energy-level alignment obtained by combining both techniques should, therefore, be regarded as a nominal approximation.

### D. UV–Vis–NIR measurements and optical modeling

UV–Vis–NIR transmission and reflection spectra were recorded using an Agilent Cary 5000 spectrophotometer. The spectral range was 250–2500 nm for transmission measurements and 350–2500 nm for reflection measurements. The measurements were used to determine the optical properties of the $MoO_x$ films and to derive the optical bandgap. For samples in which $MoO_x$ was deposited directly on glass, the measured transmission and reflection spectra were additionally used for optical modeling. The results of these samples were assigned to the others accordingly.

The modeling was performed using Code/Scout version 4.85 from W. Theiss Hardware and Software. A virtual layer stack consisting of the glass substrate and the $MoO_x$ film was constructed. The dielectric function of the $MoO_x$ film was described using a Tauc–Lorentz model. The software uses the one-dimensional transfer-matrix method to calculate the reflection and transmission of the layer stack. The parameters of the Tauc–Lorentz model were fitted to reproduce the measured transmission and reflection spectra as closely as possible. The optical bandgap of the $MoO_x$ film was extracted from the fit.

### E. Sheet-resistance measurements

The lateral sheet resistance of the $MoO_x$ films deposited directly on glass was evaluated by four-point-probe measurements using a Jandel RM3-AR measurement system.

## III. RESULTS

Kelvin probe force microscopy measurements were performed to analyze the electronic surface potential of the samples. Figure 1(a) shows a KPFM work function map of the scanned area of a ≈20 nm thick $MoO_x$ film sputtered from the ceramic target onto glass. The qualitative behavior of the measured values and their distribution is very similar for all KPFM measurements. The surface potential is rather uniform in the scanned area. Despite the slow scan rate of 0.7 Hz, a weak line-to-line variation in the slow-scan direction is visible, which is, however, small compared to the overall contrast. Furthermore, the typical amplitude of a line scan in terms of height for this sample is ~0.5 nm, which is also typical for the

04 November 2026 11:40:56

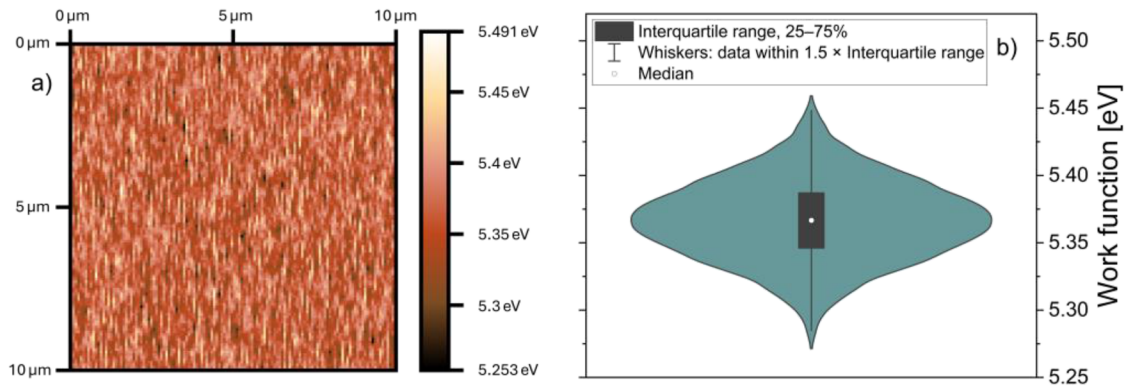



**FIG. 1.** KPFM work-function map of a $MoO_x$ sample in (a) and the corresponding work-function distribution with an embedded box-and-whisker plot in (b).


© Author(s) 2026

other samples. The layers should, therefore, be completely closed. Figure 1(b) shows a corresponding distribution of the same KPFM measurement, which is almost symmetric and normally distributed. The median is at 5.37 eV, and the standard deviation of this single measurement is 0.03 eV. Because the standard deviation is so small, it is not separately displayed as an error bar. It is important to note that this deviation refers only to the deviation within a single measurement and, therefore, does not provide any information about possible errors between different measurements. The investigated sample configurations and the corresponding work functions, including the standard deviation of the work function, valence band position from the Fermi level and the bandgap, are shown in Table I.

Figure 2 shows the sections of the normalized UPS spectra, restricted to the area of the valence band edge. The spectra are plotted as a function of binding energy relative to the Fermi level. A pronounced linear region can be identified in all measurements and

**TABLE I.** Overview of investigated $MoO_x$ samples and the extracted electronic and optical parameters.

| Mo-target | Substrate | MoOx thickness (nm) | Median work function (eV) | Work function std. dev. (eV) | Valence band maximum (eV) | Bandgap (eV) |
|---|---|---|---|---|---|---|
| Metallic | Glas | 5.4 | 5.38 | 0.03 | 3.15 | 2.78 |
| Metallic | Glas | 21.6 | 5.18 | 0.03 | 3.36 | 2.84 |
| Metallic | Glas/Ge | 5.4 | 5.19 | 0.02 | 3.08 | ··· |
| Metallic | Glas/Ge | 21.6 | 5.24 | 0.02 | 3.37 | ··· |
| Metallic | Glas/AZO | 5.4 | 5.33 | 0.02 | 2.92 | ··· |
| Metallic | Glas/AZO | 21.6 | 5.44 | 0.02 | 3.01 | ··· |
| Ceramic | Glas | 5.4 | 5.29 | 0.03 | 2.92 | 2.75 |
| Ceramic | Glas | 21.6 | 5.37 | 0.03 | 3.02 | 2.83 |
| Ceramic | Glas/Ge | 5.4 | 5.47 | 0.02 | 3.33 | ··· |
| Ceramic | Glas/Ge | 21.6 | 5.63 | 0.02 | 3.05 | ··· |
| Ceramic | Glas/AZO | 5.4 | 5.46 | 0.02 | 3.36 | ··· |
| Ceramic | Glas/AZO | 21.6 | 5.35 | 0.03 | 3.17 | ··· |

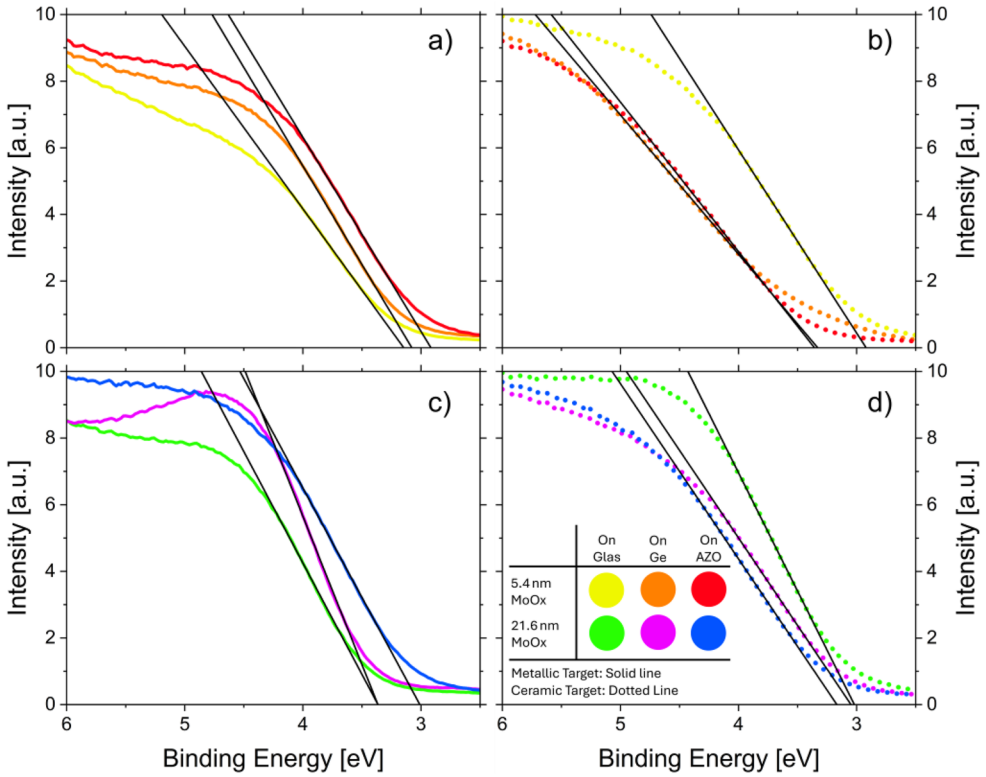



**FIG. 2.** Normalized UPS spectra of $MoO_x$ films with different thicknesses, sputter targets, and substrates: (a) 5.4 nm $MoO_x$ deposited from the metallic target, (b) 5.4 nm $MoO_x$ deposited from the ceramic target, (c) 21.6 nm $MoO_x$ deposited from the metallic target, and (d) 21.6 nm $MoO_x$ deposited from the ceramic target. Black lines represent linear fits to the valence-band onset used to determine the valence-band maximum. Binding energies are referenced to the Fermi level.

04 November 2026 11:40:56


© Author(s) 2026

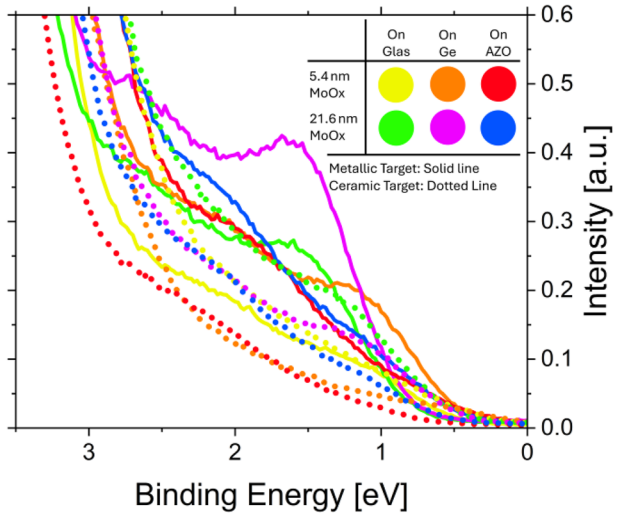



**FIG. 3.** Near-Fermi-level UPS spectra of $MoO_x$ films with different thicknesses and substrates. Energies are referenced to the Fermi level.

can be clearly distinguished from the adjacent curved regions. To determine the valence-band edge, the rising flank of the UPS signal was fitted linearly. Due to the large number of data points in the fit range and the high quality of the fit, no significant uncertainties arose. The intersection of the fitted line with the x-axis corresponds to the energy separation between the valence-band edge and the Fermi level.[27,28] All samples show a pronounced increase in photoemission intensity within the displayed energy range. The separation between the valence-band edge and the Fermi level ranges from 2.8 to 3.4 eV for the different samples. The qualitative shape of the spectra remains comparable, and the main difference is the position of the valence-band onset.

Figure 3 shows the near-Fermi-level region of the normalized UPS spectra. This enlarged region represents the left most part of the plots in Fig. 2 and permits an assessment of occupied states between the Fermi level and the valence-band edge. A weak signal intensity is observed near the Fermi energy for all samples, as expected, and increases with increasing binding energy. In addition to this onset, some samples deposited from the metallic sputtering target onto germanium, as well as the sample with the thicker $MoO_x$ film on glass, exhibit additional distinct local peaks at binding energies between 1.0 and 1.6 eV. A systematic pattern cannot be observed in the selection of samples. These peaks appear as additional near-Fermi-level, intra-gap-like states and are not part of the valence-band onset. The near-Fermi-level region, therefore, indicates that the investigated $MoO_x$ films differ not only in the energetic position of the valence-band edge but also in the density and distribution of additional occupied states within the bandgap.

Figures 4(a) and 4(b) show selected UV–Vis–NIR transmission and reflection measurements for the $MoO_x$ films, deposited using the metallic target, on glass. The fit from the optical model used to

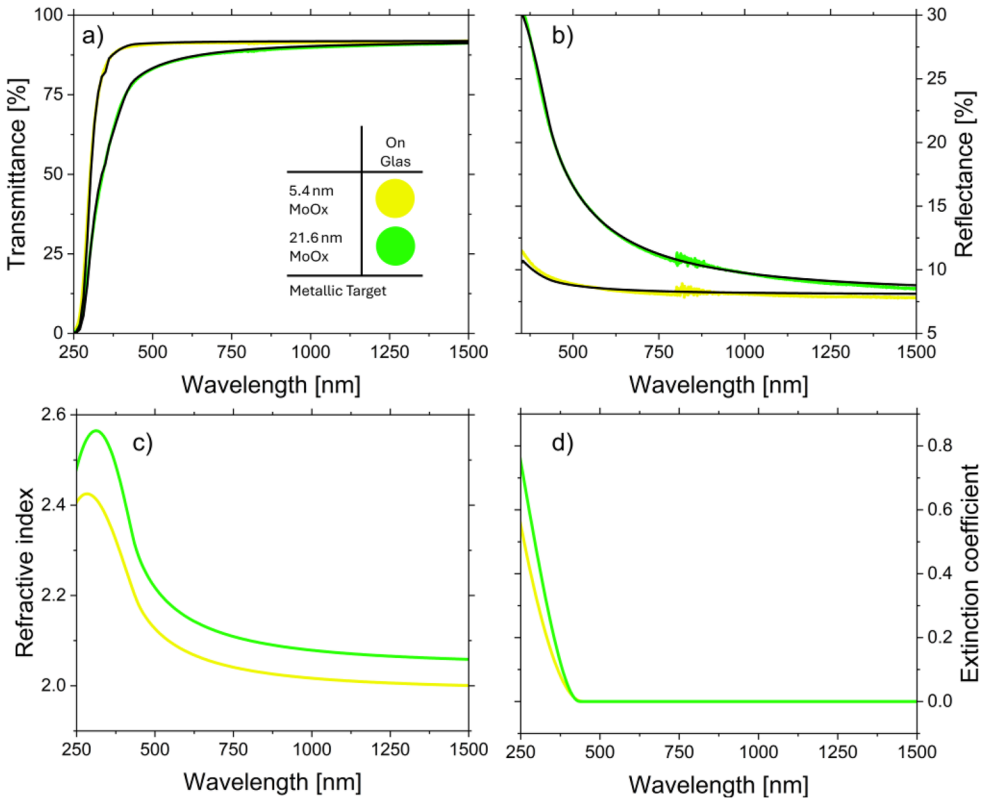



**FIG. 4.** UV–Vis transmission spectra in (a) and reflection spectra in (b), each with the dielectric-function fit shown in black, together with the refractive index in (c) and extinction coefficient in (d) derived from optical modeling.

04 November 2026 11:40:56


© Author(s) 2026

determine the dielectric function is additionally shown as a black line. The measurements of the sample with the thicker $MoO_x$ film can be clearly distinguished from those of the thinner $MoO_x$ film. As expected, the thinner film shows a larger transmittance and smaller reflectance than the thicker film for the entire spectral range.

Figures 4(c) and 4(d) show the refractive index and extinction coefficient derived from the dielectric function. The refractive-index curves are of similar shape, and both exhibit a maximum at ~325 nm. The refractive index of the thicker $MoO_x$ film is ~0.06 higher than that of the thinner film over the entire spectral range. For both samples, the extinction coefficient decreases approximately linearly with increasing wavelength and is zero from 440 to 1500 nm.

Figure 5 shows the combined results of the KPFM, UPS, and UV–Vis–NIR measurements and, thus, the energy-level structure of the $MoO_x$ films for the different samples relative to the vacuum level. The Fermi level $E_{Fermi} = -\Phi$ relative to vacuum was obtained from the KPFM work function, the valence-band position $E_{Valence}$ was obtained by combining this work function with the UPS onset $E_{UPS\text{-}Onset}$ ($E_{Valence} = E_{Fermi} - E_{UPS\text{-}Onset}$), and the conduction-band position $E_{Conduction}$ was derived by adding the optically determined bandgap $E_{Bandgap}$ to the valence-band position ($E_{Conduction} = E_{Fermi} - E_{UPS\text{-}Onset} + E_{Bandgap}$). Each vertical set of levels represents the energy scheme of one sample. The corresponding sample structures are shown schematically in the lower part of the figure.

For all samples, the valence band lies deep relative to the vacuum level, in the range from −8.0 eV to −8.8 eV. Based on the nominal values obtained from the UPS valence-band onset and the optically determined bandgap, $E_{Fermi} - E_{Conduction}$ ranges from ~0.1 to 0.5 eV. Thus, the Fermi level is nominally located close to or above the derived conduction-band edge.

No clear systematic dependence of the nominal energy levels on the investigated deposition parameters is evident. Neither the $MoO_x$ thickness, which varied between 5.4 and 21.6 nm, nor the use of a metallic Mo target in a reactive process or a ceramic $MoO_x$ target leads to a clear systematic shift of the energy levels. Similarly, the presence of an additional germanium or AZO layer beneath the $MoO_x$ does not strongly alter the resulting energy scheme. This suggests that the surface electronic structure is governed mainly by the $MoO_x$ layer itself rather than by the underlying substrate. In particular, the similarity of $MoO_x$ on glass, germanium, and AZO suggests that the Fermi-level position is governed by a mechanism within the $MoO_x$, most likely related to intrinsic defect states and oxygen nonstoichiometry. However, because KPFM is a surface-sensitive technique, this conclusion primarily applies to the near-surface region of the $MoO_x$ films.

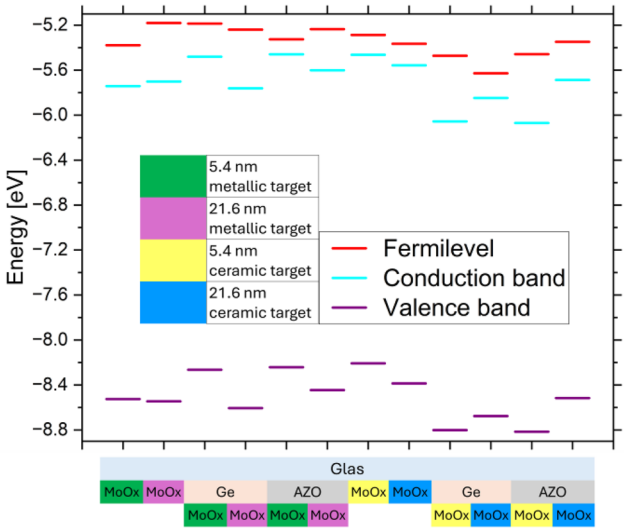



**FIG. 5.** Energy levels determined for $MoO_x$ films on different substrates and with different film thicknesses, referenced to the vacuum level.

## IV. DISCUSSION

The magnetron-sputtered $MoO_x$ has been studied to analyze its optoelectronic properties. The films show a broadly similar energy-level structure across the different thicknesses, sputter conditions, and substrates that have been used. In all cases, the Fermi level is located close to, or nominally above, the derived conduction-band edge.

Given the position of the Fermi level, the studied $MoO_x$ films might be expected to exhibit metallic behavior. In a conventional crystalline semiconductor with delocalized parabolic bands, such an energetic configuration would correspond to degenerate n-type doping and should result in a high density of free electrons and measurable electrical conductivity. This is not observed here. Four-point-probe measurements on $MoO_x$ films deposited directly on glass did not yield a measurable conductivity inside the measurement range. Therefore, the constructed energy diagram cannot be interpreted as that of a simple crystalline metal or degenerately doped semiconductor.

Unlike UPS, which is performed under UHV conditions, KPFM measurements are performed under ambient air. This raises the question of whether adsorbed water has any significant influence on the measured work function. Wrana *et al.* found an effect of 0.2 eV for adsorbed surface species on a TiO metal oxide under ambient KPFM measurements.[29] This would suggest that the effect is rather small. Moreover, this circumstance should not affect the energy level differences, since it only shifts the entirety of them and should affect all samples equally. Accordingly, the effect does not influence $E_{Fermi} - E_{Conduction}$ because this quantity is determined from the UPS valence-band onset and the optical bandgap and is, therefore, independent of the KPFM work function.

The optical bandgap was determined only for $MoO_x$ on glass substrates. This raises the question if substrate induced differences in film growth for the Ge and AZO substrates can be expected, ultimately altering electro-optical properties. The fitting of UV–Vis measurements was restricted to $MoO_x$ films on glass because the additional Ge or AZO layers dominate the optical response of the multilayer stacks and prevent a reliable independent extraction of the $MoO_x$ dielectric function and bandgap. Since the sputtered Ge layer is amorphous and does, therefore, not provide a crystalline template, no differences to the glass substrate are expected.[1] However, sputtered AZO could be present in a polycrystalline structure, which could change the growth of $MoO_x$.[1,30] In combination with the absence of a clear substrate-dependent trend in the KPFM and UPS results, this suggests that large changes in the $MoO_x$ bandgap cannot be excluded but remain unlikely.

04 November 2026 11:40:56


© Author(s) 2026

Most importantly, the discussed points above do not change the central physical statement of this study. The exact sign of $E_{Fermi} - E_{Conduction}$ cannot be resolved reliably for nominal separations of only about 0.1 eV. The relevant observation is that the Fermi level lies close to the derived conduction-band edge, which would normally result in a metallic like conduction. This is not what we have measured in our lateral conductivity measurements. This conclusion is already drawn for the $MoO_x$/glass samples, where the optical bandgap was determined directly.

Coming back to the discussion of the electronic structure, especially the substoichiometric and amorphous $MoO_x$ character, has to be considered. As described in the Introduction, $MoO_x$ is known to contain oxygen-vacancy-related defect states within the bandgap. Battaglia *et al.* report $MoO_x$ as a high-work-function material with a low density of states at the Fermi level originating from the tail of an oxygen-vacancy-derived defect band within the bandgap.[9] They also reported that $MoO_x$ can act as a hole-selective contact even though its electronic structure differs from that of a simple wide-bandgap semiconductor.[9] In the same work, defect features were assigned to oxygen vacancies and Mo 4d-derived states. Importantly, the O 2p-derived valence-band edge did not shift significantly upon the creation or annihilation of oxygen vacancies, indicating that these vacancies do not behave as conventional shallow donors in $MoO_x$.[9] Thus, the defects do not primarily provide free charge carriers for lateral transport.

The additional states near the Fermi level are qualitatively consistent with defect-related states reported for $MoO_x$. Battaglia *et al.* reported defect states in thin $MoO_x$ films at an energy of 1 eV below the Fermi level, which were attributed primarily to oxygen vacancies.[9] Scirè *et al.* likewise reported a defect band or additional defect features at ~1.1 and 1.2 eV below the conduction band.[21] In that study, the defect states were also associated with oxygen vacancies. These energy values are not directly equivalent because the former are UPS binding energies referenced to the Fermi level, whereas the latter are defect positions referenced to the conduction-band edge and were obtained from optical analysis. Nevertheless, the comparable energy scale supports an assignment of the observed UPS features to occupied defect-related states.

This distinction is crucial for the interpretation of the present data. The conduction-band edge shown in Fig. 5 is derived from an optical bandgap and should be understood as an effective band edge rather than as a direct measurement of extended conducting states. In amorphous and defect-rich oxides, band tails and localized defect states can extend into the nominal gap. As a result, the Fermi level may appear energetically close to the conduction band or even above an optically extrapolated conduction-band edge, while the electronic states at the Fermi level remain localized. Metallic conduction, however, requires delocalized states at the Fermi level that extend across the sample.[31]

The defect band mentioned above, located ~1.1 eV below the conduction-band edge, is relevant in the context of silicon heterojunction solar cells. Such defect states have been discussed as important for trap-assisted tunneling, whereas the wide bandgap and band alignment of $MoO_x$ provide electron blocking and hole selectivity.[21,32–34] Thus, defect states in $MoO_x$ do not necessarily imply metallic conduction. Instead, they can provide localized intermediate states that assist vertical charge transfer across a contact layer only a few nanometers thick.

Four-point-probe measurements were performed on the $MoO_x$ samples deposited directly on glass. For none of the samples could a conductivity within the measurement range of the instrument be obtained. This observation is consistent with literature values for highly oxidized $MoO_x$ or $MoO_3$. Using the transfer-length method, Gerling *et al.* determined a sheet resistance of $\sim 5 \times 10^{12}$ Ω/□ for 15-nm-thick thermally evaporated $MoO_3$ films on glass.[7] This value is well above the measurement range of the instrument used here, for which a range from $10^{-3}$ Ω/□ to $5 \times 10^{8}$ Ω/□ is specified.[35]

This supports the previous measurement that the lateral sheet resistance of the present $MoO_x$ films lies above the accessible measurement range.

A comparison with sputtered $MoO_x$ films further shows that measurable sheet resistances occur primarily in substantially more reduced films. He *et al.* reported a strong dependence on oxygen content for 400-nm-thick reactively sputtered $MoO_x$ films.[36] A sheet resistance of 120 Ω/□ was measured for oxygen-poor films, whereas the sheet resistance increased strongly at higher oxygen contents and also exceeded the measurement range.

Oh *et al.* likewise reported very low resistivities for strongly reduced, post-treated $MoO_x$ films, which were associated with the formation of a $MoO_2$-rich phase.[37] By contrast, the absence of measurable lateral conductivity in the thin $MoO_x$ films investigated here argues against a continuous metallic or $MoO_2$-like transport pathway.

The absence of measurable conductivity is, therefore, not in conflict with the use of $MoO_x$ as a hole-selective contact. On the contrary, it supports the picture that the sputtered $MoO_x$ films analyzed here do not show metallic conductivity, even though the constructed energy diagram places the Fermi level close to the conduction-band edge. The relevant states near the Fermi level are likely localized defect or band-tail states rather than extended conduction-band states. This interpretation is also consistent with the four-point-probe results because such states do not give rise to extended metallic conduction-band transport. This may also explain why no pronounced dependence on thickness, substrate, or target material is observed. If the near-surface Fermi level is predominantly influenced by a similar distribution of oxygen-vacancy-related states in all samples, moderate variations in the underlying layer stack or deposition route may shift the absolute energy levels only weakly.

These states may be beneficial for charge extraction if their density is sufficient to support trap-assisted transport, but excessive defect densities may also increase recombination or lead to unfavorable transport barriers.[38,39] Therefore, the role of defects is ambivalent. They can enable contact functionality, but they do not necessarily produce high conductivity and may become detrimental if their density or energetic distribution is not controlled.

Overall, the results indicate that sputtered $MoO_x$ forms a high-work-function, wide bandgap contact material whose energy levels are only weakly affected by the investigated film thicknesses, substrates, and target materials. The position of the Fermi level near or above the derived conduction-band edge should not be interpreted as evidence for metallic conductivity in $MoO_x$. Instead, the data are more consistently explained by a disordered oxide with localized

04 November 2026 11:40:56


© Author(s) 2026

defect and band-tail states, while the extended-state conductivity remains low. This reconciles the constructed energy diagram, the absence of measurable lateral conductivity, and the established use of $MoO_x$ as a hole-selective contact in solar cells.

## V. SUMMARY AND CONCLUSION

In this work, the electronic and optical properties of magnetron-sputtered $MoO_x$ thin films were investigated by using KPFM, UPS, UV–Vis–NIR spectroscopy, and four-point probe measurements. Using these measurements, it was possible to analyze the energy levels of different sputtered $MoO_x$ thin films and thereby gain insights into the transport mechanism of charge-carrier-selective contact materials. Within the present sample set, no clear systematic dependence of the nominal energy-level alignment on $MoO_x$ thickness, sputter target, and underlying glass, Ge, or AZO layer was observed. This indicates that the near-surface electronic structure is comparatively robust with respect to the investigated sample configurations.

The Fermi level was found to lie slightly above the conduction-band edge derived from the UPS valence-band position and the optical bandgap. However, no measurable lateral conductivity was obtained for the $MoO_x$ films deposited directly on glass. The apparent discrepancy between the energy-level diagram and conductivity is consistently explained by a disordered electronic structure containing localized defect and band-tail states rather than extended metallic states. Additional UPS peaks within the bandgap support the presence of occupied defect states, most likely associated with oxygen deficiency and reduced Mo centers. These states may contribute to defect-assisted vertical charge transfer without producing metallic lateral transport. Overall, the results provide a consistent description of sputtered $MoO_x$ as a high-work-function, wide-bandgap, and electrically resistive material whose defect-mediated electronic structure is compatible with its use as a hole-selective contact. The material exhibits robust properties with respect to the sputtering parameters and appears suitable for incorporation into a solar cell. This represents another important step toward a fully sputtered transparent thin-film solar cell without dopant dependent contact materials.

## ACKNOWLEDGMENTS

This study continues research that was previously funded by the research program "Zukunft Bau Forschungsförderung," provided by the German Federal Institute for Research on Building, Urban Affairs, and Spatial Development on behalf of the Federal Ministry for Housing, Urban Development, and Building (10.08.18.7-22.36). The ultraviolet photoelectron spectroscopy measurements were made possible by DFG funding through INST 184/144-1 FUGG.

## AUTHOR DECLARATIONS

### Conflict of Interest

The authors have no conflicts to disclose.

### Author Contributions

**Nico Ruskaup**: Conceptualization (equal); Data curation (lead); Formal analysis (lead); Investigation (lead); Methodology (lead); Validation (lead); Visualization (lead); Writing – original draft (lead); Writing – review & editing (equal). **Konstantin Rücker**: Data curation (supporting); Investigation (supporting); Writing – review & editing (supporting). **Kai Gehrke**: Conceptualization (equal); Funding acquisition (lead); Project administration (lead); Supervision (equal); Writing – review & editing (equal). **Stephan Heise**: Conceptualization (equal); Supervision (equal); Writing – review & editing (supporting). **Martin Vehse**: Conceptualization (equal); Funding acquisition (supporting); Project administration (supporting); Supervision (equal); Writing – review & editing (supporting).

## DATA AVAILABILITY

The data that support the findings of this study are available from the corresponding author upon reasonable request.

## REFERENCES

[1] N. Ruskaup, K. Gehrke, S. Heise, M. Vehse, and C. Agert, J. Vac. Sci. Technol., A **43**, 063407 (2025).
[2] W.-D. Dachselt, W.-D. Munz, and M. Scherer, "Low emissivity and solar control coatings on architectural glass," SPIE **324**, 37–43 (1982).
[3] H. J. Gläser, *Dünnfilmtechnologie auf Flachglas* (Hofmann-Verlag, Schorndorf, 1999).
[4] N. Ruskaup, K. Gehrke, S. Heise, and M. Vehse, Opt. Express **34**, 7701–7714 (2026).
[5] J. Ibarra Michel, J. Dréon, M. Boccard, J. Bullock, and B. Macco, Prog. Photovoltaics Res. Appl. **31**, 380–413 (2023).
[6] L. V. Hublikar, S. V. Ganachari, F. A. Shilar, and N. Raghavendra, Mater. Res. Bull. **187**, 113351 (2025).
[7] L. Gerling, S. Mahato, C. Voz, R. Alcubilla, and J. Puigdollers, Appl. Sci. **5**, 695–705 (2015).
[8] J. Bullock, A. Cuevas, T. Allen, and C. Battaglia, Appl. Phys. Lett. **105**, 232109 (2014).
[9] C. Battaglia, X. Yin, M. Zheng, I. D. Sharp, T. Chen, S. McDonnell, A. Azcatl, C. Carraro, B. Ma, R. Maboudian, R. M. Wallace, and A. Javey, Nano Lett. **14**, 967–971 (2014).
[10] C. Battaglia, S. M. de Nicolás, S. de Wolf, X. Yin, M. Zheng, C. Ballif, and A. Javey, Appl. Phys. Lett. **104**, 113902 (2014).
[11] Y. Guo and J. Robertson, Appl. Phys. Lett. **105**, 222110 (2014).
[12] S. K. C., R. C. Longo, R. Addou, R. M. Wallace, and K. Cho, Sci. Rep. **6**, 33562 (2016).
[13] H. Hou, W. Wang, Q. Kang, J. Wang, Z. Chen, Y. Wang, Y. Cui, Y. Yu, J. Zhu, H. Yan, and J. Hou, Nano Energy **131**, 110173 (2024).
[14] M. Bivour, J. Temmler, F. Zahringer, S. Glunz, and M. Hermle, in *2016 IEEE 43rd Photovoltaic Specialists Conference (PVSC)* (IEEE, 2016), pp. 215–220.
[15] J. Meyer, S. Hamwi, M. Kröger, W. Kowalsky, T. Riedl, and A. Kahn, Adv. Mater. **24**, 5408–5427 (2012).
[16] V. Shrotriya, G. Li, Y. Yao, C.-W. Chu, and Y. Yang, Appl. Phys. Lett. **88**, 73508 (2006).
[17] A. Kumar, S. Tomer, Vandana, T. Fix, M. Dutta, S. K. Srivastava, and P. Pathi, J. Phys. D: Appl. Phys. **57**, 505105 (2024).
[18] B. K. Keerthana, C. Rahul, J. Kumari, and P. Agarwal, J. Mater. Sci.: Mater. Electron. **37**, 1406 (2026).
[19] K. Inzani, T. Grande, F. Vullum-Bruer, and S. M. Selbach, J. Phys. Chem. C **120**, 8959–8968 (2016).

04 November 2026 11:40:56


© Author(s) 2026

[20]K. Inzani, M. Nematollahi, F. Vullum-Bruer, T. Grande, T. W. Reenaas, and S. M. Selbach, Phys. Chem. Chem. Phys. **19**, 9232–9245 (2017).
[21]D. Scirè, P. Procel, A. Gulino, O. Isabella, M. Zeman, and I. Crupi, Nano Res. **13**, 3416–3424 (2020).
[22]Y. Jiang, S. Cao, L. Lu, G. Du, Y. Lin, J. Wang, L. Yang, W. Zhu, and D. Li, Nanoscale Res. Lett. **16**, 87 (2021).
[23]M. Bivour, B. Macco, J. Temmler, W. M. M. E. Kessels, and M. Hermle, Energy Proc. **92**, 443–449 (2016).
[24]J. Sun, Q. Zheng, S. Cheng, H. Zhou, Y. Lai, and J. Yu, J. Mater. Sci.: Mater. Electron. **27**, 3245–3249 (2016).
[25]P. H. Mayrhofer, F. Kunc, J. Musil, and C. Mitterer, Thin Solid Films **415**, 151–159 (2002).
[26]K. Fuchs, P. Rödhammer, E. Bertel, F. P. Netzer, and E. Gornik, Thin Solid Films **151**, 383–395 (1987).
[27]L. A. H. Jones, Z. Xing, J. E. N. Swallow, H. Shiel, T. J. Featherstone, M. J. Smiles, N. Fleck, P. K. Thakur, T.-L. Lee, L. J. Hardwick, D. O. Scanlon, A. Regoutz, T. D. Veal, and V. R. Dhanak, J. Phys. Chem. C **126**, 21022–21033 (2022).
[28]V. L. Colvin, A. P. Alivisatos, and J. G. Tobin, Phys. Rev. Lett. **66**, 2786–2789 (1991).
[29]D. Wrana, K. Cieślik, W. Belza, C. Rodenbücher, K. Szot, and F. Krok, Beilstein J. Nanotechnol. **10**, 1596–1607 (2019).
[30]M. Chaves, R. Ramos, E. Martins, E. C. Rangel, N. C. Da Cruz, S. F. Durrant, and J. R. R. Bortoleto, Mat. Res. **22**, 15 (2019).
[31]N. F. Mott, Philos. Mag. **17**, 1259–1268 (1968).
[32]D. Chen, M. Gao, Y. Wan, Y. Li, H. Guo, and Z. Ma, Appl. Surf. Sci. **473**, 20–24 (2019).
[33]J. Melskens, A. Schnegg, A. Baldansuren, K. Lips, M. P. Plokker, S. W. H. Eijt, H. Schut, M. Fischer, M. Zeman, and A. H. M. Smets, Phys. Rev. B **91**, 245207 (2015).
[34]R. Maurya, N. Dsouza, A. K. Singh, N. Bandaru, R. Kanakala, M. Seraj Uddin, R. Madaka, S. C. Roy, and J. K. Rath, Mater. Today: Proc. **104**, 53–57 (2024).
[35]Bridge Technology, CYL-RM3AR Four Point Probe System: General Purpose Portable Four Point Probing System for Measuring Sheet Resistance or Volume Resistivity (Product Brochure Jandel Engineering Ltd,) [Online]. Available: https://www.four-point-probes.com/cyl+rm3ar.pdf
[36]F. He, X. Yin, J. Li, S. Lin, L. Wu, X. Hao, J. Zhang, and L. Feng, Vacuum **176**, 109337 (2020).
[37]M. Sook Oh, B. Seob Yang, J. Ho Lee, S. Ha Oh, U. Soo Lee, Y. Jang Kim, H. Joon Kim, and M. Soo Huh, J. Vac. Sci. Technol. A **30**, 31501 (2012).
[38]R. García-Hernansanz, E. García-Hemme, D. Montero, J. Olea, A. Del Prado, I. Mártil, C. Voz, L. G. Gerling, J. Puigdollers, and R. Alcubilla, Sol. Energy Mater. Sol. Cells **185**, 61–65 (2018).
[39]C. Messmer, M. Bivour, J. Schön, and M. Hermle, J. Appl. Phys. **124**, 85702 (2018).

04 November 2026 11:40:56


© Author(s) 2026